



Nanoindentation in multi-modal map combinations: a correlative approach to local mechanical property assessment

Christopher M. Magazzeni^{1,a)} , Hazel M. Gardner¹, Inigo Howe¹, Phillip Gopon², John C. Waite¹, David Rugg³, David E. J. Armstrong¹, Angus J. Wilkinson¹

¹Department of Materials, University of Oxford, Parks Road, Oxford OX1 3PH, UK

²Department of Earth Sciences, University of Oxford, S Parks Rd, Oxford OX1 3AN, UK

³Rolls-Royce plc, Elton Rd, Allenton DE24 8ED, Derby, UK

^{a)}Address all correspondence to this author. e-mail: christopher.magazzeni@materials.ox.ac.uk

Received: 27 August 2020; accepted: 30 November 2020 ; published online: 4 January 2021

A method is presented for the registration and correlation of property maps of materials, including data from nanoindentation hardness, Electron Back-Scattered Diffraction (EBSD), and Electron Micro-Probe Analysis (EPMA). This highly spatially resolved method allows for the study of micron-scale microstructural features, and has the capability to rapidly extract correlations between multiple features of interest from datasets containing thousands of data points. Two case studies are presented in commercially pure (CP) titanium: in the first instance, the effect of crystal anisotropy on measured hardness and, in the second instance, the effect of an oxygen diffusion layer on hardness. The independently collected property maps are registered using affine geometric transformations and are interpolated to allow for direct correlation. The results show strong agreement with trends observed in the literature, as well as providing a large dataset to facilitate future statistical analysis of microstructure-dependent mechanisms.

Introduction

Over the past decades, significant advances have been made in techniques used to determine material properties on an ever finer length scale, allowing for a better understanding of basic material property–microstructure relationships [1–3]. These developments have provided crucial insight into fundamental materials science, facilitating more accurate multi-scale modelling [4–10], as well as the necessary property assessment for modern manufacturing processes with small features [11–16].

Researchers have used crystallographic techniques [3, 17–20], composition measurements [21–25], and nanoindentation [21, 26, 27] amongst a variety of other techniques to determine local properties. As microstructural feature sizes become smaller, and systems more complex, there is a need for a distributed approach to understanding how multiple factors

may affect one another, and in turn affect the viability of parts in complex service environments [21, 28].

Recent developments in nanoindentation instrumentation have enabled a wide range of experimental procedures, including more complex loading and sensing regimes such as strain-rate experiments to measure the effect of indentation rate [29–31], and more complex specimen preparation techniques such as micro-pillar compression to isolate microstructural features [32–36]. A recent addition to the tools available for local mechanical property assessment has been the development of rapid nanoindentation mapping: mechanical property maps of hardness and modulus can be obtained that resolve micron-scale microstructural features [37–39], and create, at an unprecedented rate, large datasets for statistical analysis [40].

Work carried out using this technique has shown developments in distinguishing between phases in cement [40, 41], or

dissimilar material coatings [38] through indentation alone and has enabled the collection of statistically significant datasets [38, 41–46]. Statistical clustering methods are available to classify data points and extract characteristic properties from a finite set of discrete phases. However, in microstructures where changes in local property are continuous, or are within a few tens of percent, alternative approaches requiring additional source signals need to be developed in order to de-convolute more nuanced structure–property relationships. There is scope to collect multi-dimensional datasets from microstructurally rich materials that combine chemical, crystallographic, and mechanical data at high resolution. However, the challenge remains to correctly collect, correct, align, and correlate these very different properties.

Nanoindentation mapping contains an inherent trade-off between resolution and accuracy, manifested as the trade-off between indent spacing and depth. Deeper indents generally provide higher accuracy data of material bulk properties [47] though care must be taken when spacing indents close to one another as the plastic zone of one indent can affect the result of the second. This depth-to-spacing ratio has been discussed by Sudharshan Phani et al. [37], where a ratio of depth to spacing of 1:10 is recommended in nanoindentation maps. This directive on depth-to-spacing ratios alone does not imply any resolution limit in nanoindentation mapping. However, in combination with the above statement on shallow indent accuracy, the trade-off is the smaller the indentation spacing, the larger the error in the data. This is either due to depth-to-spacing ratios approaching or lying below the above recommendation, or due to surface effects at shallow depths affecting bulk material hardness measurement [47]. Some experiments indicate that for nanoindents approximately 100 nm in depth, this error for each indent is larger than the error from decreasing the depth-to-spacing ratio, justifying the use of a 1:7 ratio for certain experiments where high spatial resolution is desired.

In this paper, we present a method for directly correlating crystallographic data from Electron BackScatter Diffraction (EBSD), chemical data from Wavelength Dispersive Spectroscopy (WDS) of X-rays, and mechanical properties data from nanoindentation. From this we study variations in mechanical response as a function of crystal orientation, interstitial content (in the case presented, oxygen content), and spatial position, rather than simple characteristic properties for a small number of discrete phases. We illustrate the method and analysis possible using titanium test specimens, showing the first steps in rapidly obtaining structure property relations from complex systems at high resolution. We present two commercially pure titanium systems to be mapped and correlated: the first with a bulk un-textured alpha microstructure, and the second with an oxygen surface diffusion layer.

Results

Dataset 0—nanoindentation comparisons and tip calibration persistence

Figure 1 shows data from the nanoindentation map performed on the fused silica reference material, illustrating tip calibration persistence. The map, where each indent corresponds to one pixel, was constructed of 3×3 bundles, starting from the bottom-right of the image, and progressively moving up in a serpentine motion starting in the negative x -direction. A graphical representation of this strategy is provided in the supplemental information in Fig. 9.

In Fig. 1a and b it can be seen that there is an inaccuracy in the stage movement travelling between bundles: the horizontal lines of high modulus correspond to indents more closely spaced than programmed. The collection strategy within bundles can also be seen, with vertical stripes corresponding to systematic errors in x -stage positioning within bundles. These factors contribute to noise in the nanoindentation mapping, but do not prevent the extraction of trends from the full map.

Histograms of the modulus and hardness values for the entire map are shown in Fig. 1c and d. The mean modulus is 12.5% higher than the value of 72 GPa established using slower standard CSM mode nanoindentation (more discussion of this offset in hardness will be given later). However, it is reassuring that there is minimal increase in modulus or hardness across the bundles, indicating little tip wear within a map of this size.

The CSM data shown in Fig. 1e and f support this conclusion. The first set of nine indents made before mapping were used for calibration, while the second set obtained after mapping show little to no change in modulus, ~ 2 GPa, at the 150 nm depth used for the indentation mapping. This indicates there is no significant systematic change in tip calibration during the indentation mapping.

Further to discussions of tip calibration persistence, it is necessary to consider the spatial resolution of this mapping technique. We compare results obtained using conventional CSM nanoindentation measurements and nanoindentation mapping on the same material. Figures 10 and 11 in Supplementary Information provide an example of the discrepancy between nanoindentation mapping and CSM nanoindentation results for a fused silica calibration specimen and the CP titanium specimen studied. There is a persistent artificial increase in hardness and modulus recorded when performing nanoindentation mapping, which decreases as depth is increased. This may be related to the rate at which the indents were performed, or due to the difference in the way these values are calculated. Despite these systematic variations, nanoindentation mapping provides data in line with literature accepted values for fused silica.

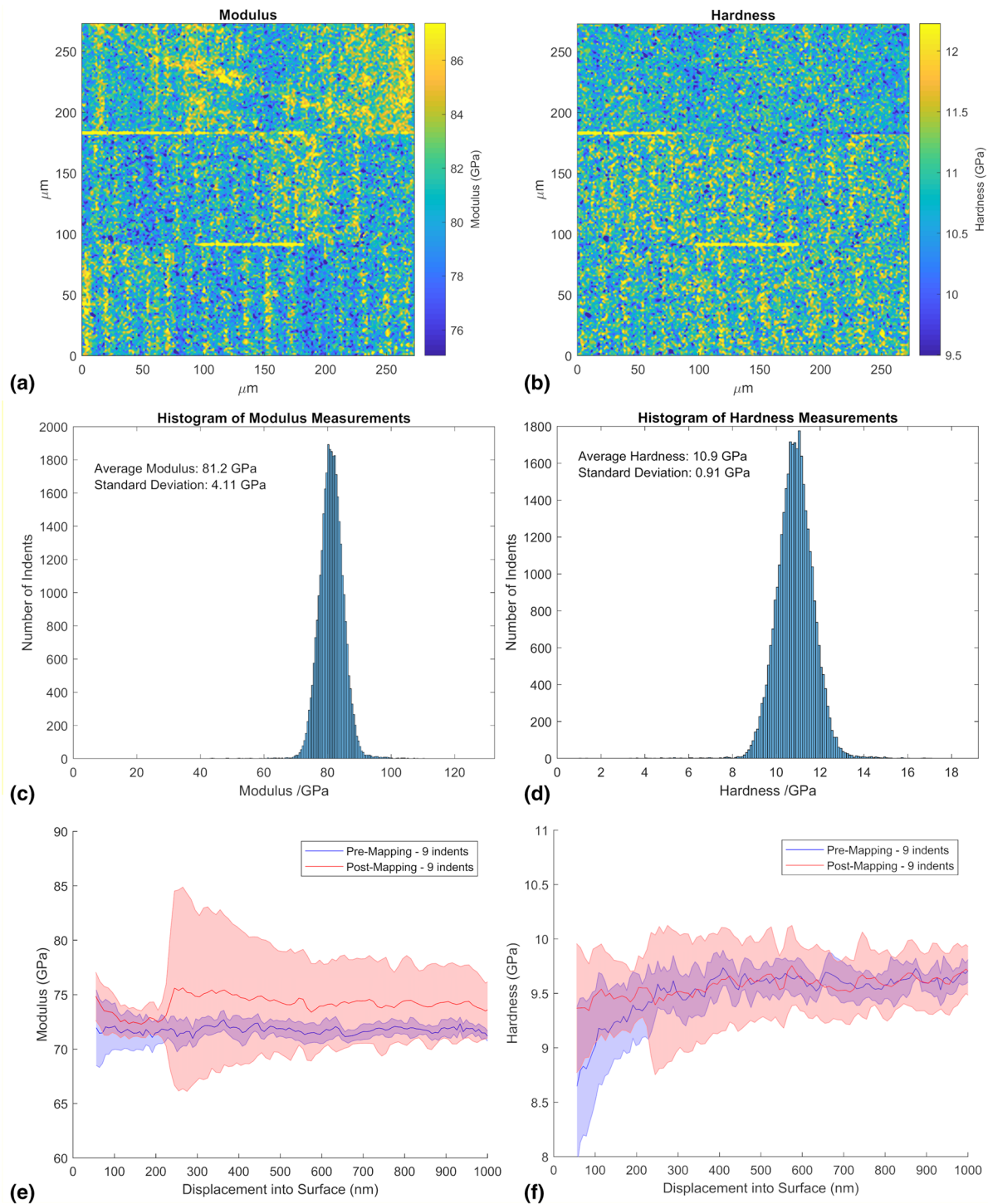


Figure 1: Modulus (a) and hardness (b) figure of nanoindentation map on Fused Silica. Indents are performed at 3 mN, spaced 1.5 μm apart. This corresponds to a depth/spacing ratio of 1:10, with indents approximately 150 nm deep. Histograms of modulus (c) and hardness (d) maps obtained in (a, b). CSM nanoindentation data corresponding to modulus (e) and hardness (f) both before (blue) and after (red) performing the nanoindentation map. The large increase in error after ca. 200 nm is likely due to a particle lodged in the tip during mapping at this depth: this increase was observed only in the first of the nine indents, and corresponds to a depth slightly beyond that achieved during the mapping.

Dataset 1

Figure 2 shows EBSD data obtained from the commercially pure titanium specimen which has grains with a mean size of

approximately 15 μm with weak texture allowing for a full range of orientations to be probed. A nanoindentation map was then

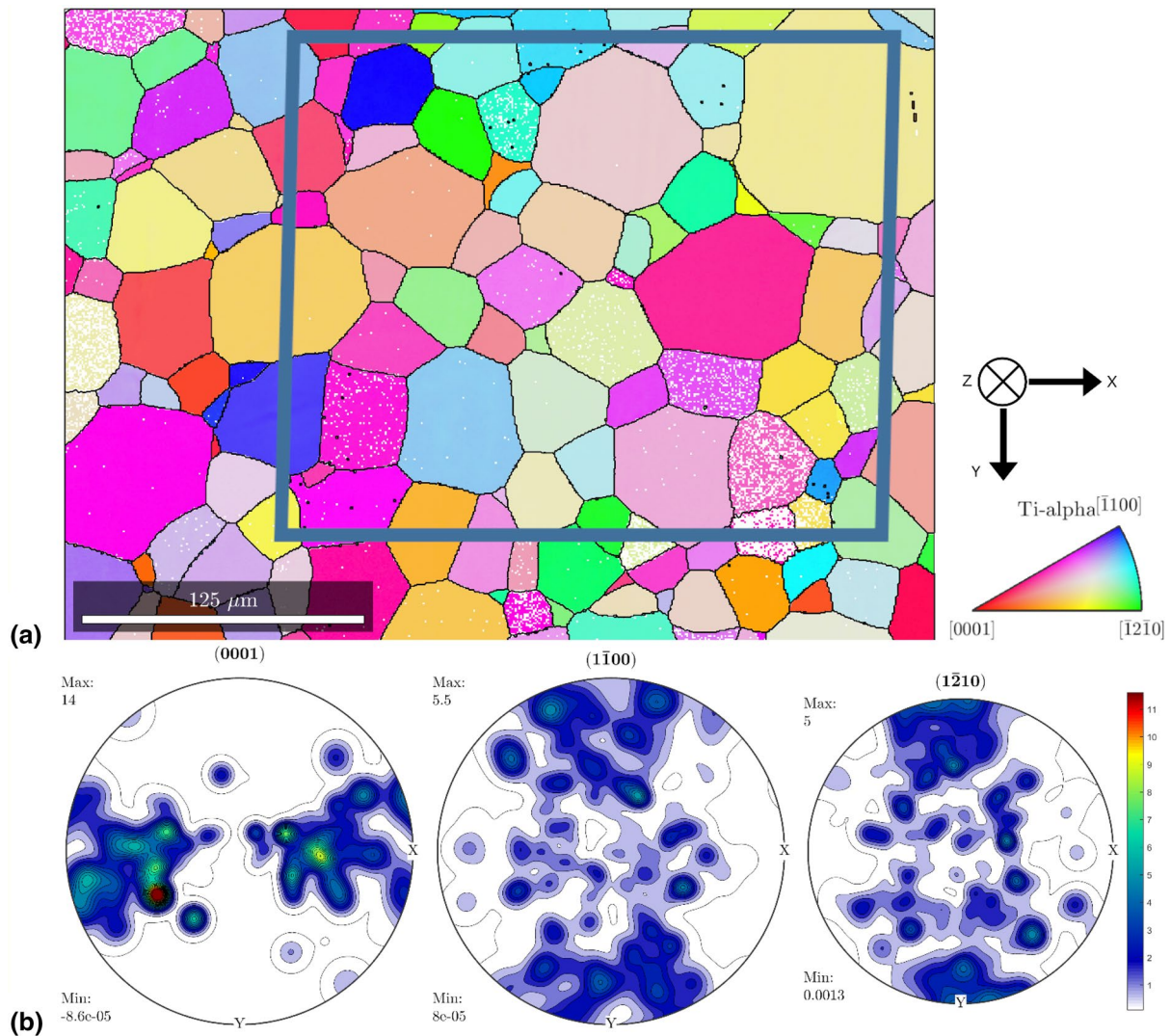


Figure 2: (a) IPFZ EBSD map of the CP titanium specimen with pole key and (b) pole figure. Overlay indicates the approximate area to be nanoindented.

performed on the specimen within the region mapped by EBSD, with results shown in Fig. 3.

The hardness map in Fig. 3 reveals significant contrast between grains, whereas there is lower grain-to-grain contrast in the modulus map, relative to the noise. We note the dissimilarity in contrast between hardness and modulus maps in Fig. 3, in contradiction to previous reports of this well-studied material [20], which points to a more complex relationship between the two. As a consequence, the rest of this paper discusses only the hardness data in order to remain confident in the trends observed. This difference between the hardness and modulus maps is discussed further in the nanoindentation mapping methods section.

An affine transformation was performed in order to correctly align the EBSD map to the nanoindentation map using a set of eight triple junction points in these maps, as highlighted in Fig. 12 (Supplementary Information). Once aligned, the two maps can be interpolated to the same size, so that correlations between various property fields can be undertaken easily. To down-scale the EBSD map, nearest-neighbour interpolation is used, a decision which is discussed in Limitations and Methods. For consistency, we use the same colour scheme for EBSD derived maps as for nanoindentation derived ones.

The crystal orientation data are readily simplified to display maps of the declination angle between the basal plane normal (i.e. the *c*-axis) and the surface normal (i.e. indentation

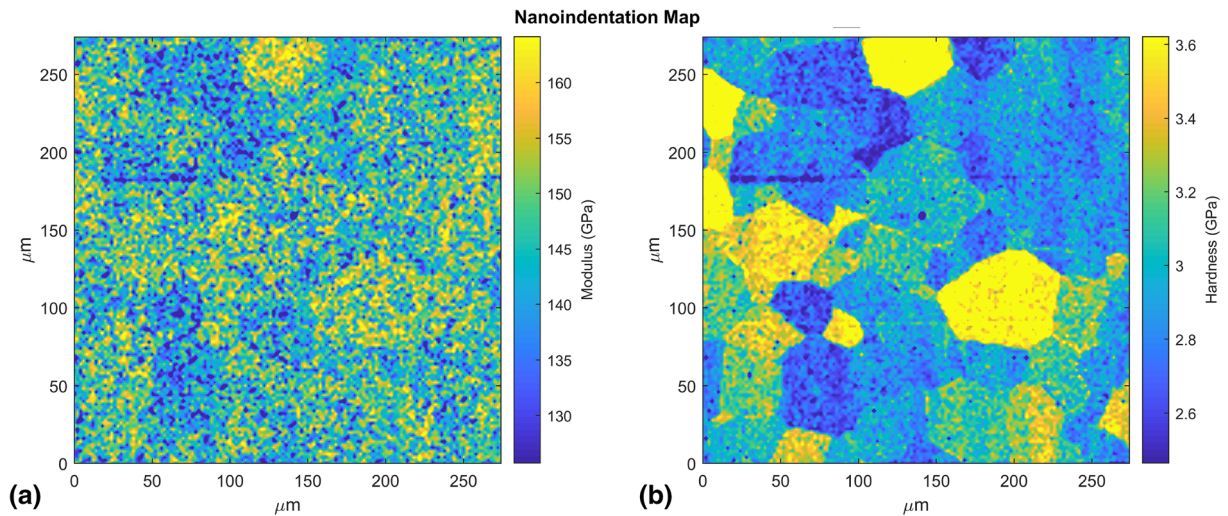


Figure 3: Nanoindentation map of CP titanium showing (a) modulus and (b) hardness. The indentation map was performed at a fixed load of 3 mN corresponding to an approximate depth of 200 nm and an indent spacing of 2 μm . The map is 138 \times 138 pixels or indents in size, corresponding to 19,044 data points.

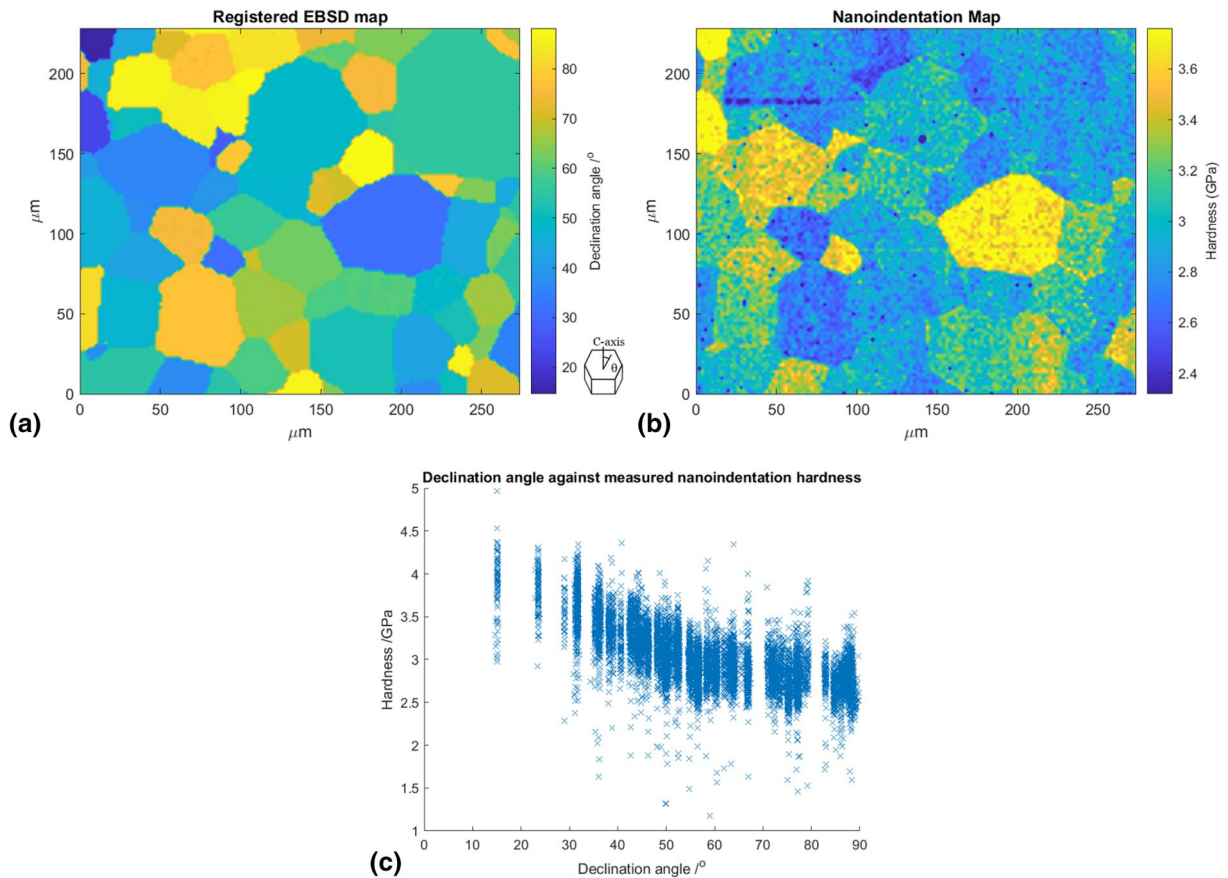


Figure 4: (a) Registered EBSD declination angle map, (b) nanoindentation obtained hardness map, and (c) a scatter plot of declination angle, measured through EBSD, against nanoindentation measured hardness using all 15,594 data points.

direction), as seen in Fig. 12 (Supplementary Information). This is done as commercially pure titanium crystals are well understood to have high crystal anisotropy due to changes in

the declination angle [20, 48, 49]. In Fig. 4a and b, the map of declination angle has been aligned to the nanoindentation

map, allowing direct comparison between the two maps since the spatial sampling is now equal.

These arrays can now be used to create scatter plots relating pixel-by-pixel the declination angle of the *c*-axis to the measured hardness, shown in Fig. 4c.

This curve closely resembles that reported in previous experiments, notably by Britton et al. [20]: the anisotropic effect of declination angle on measured nanoindentation hardness is clearly evident, and the range of hardness (~ 1 GPa) can be used to validate these results. The benefit of this technique lies beyond the immediately visible: a very large quantity of data (> 10,000 data points) has been collected in a relatively short time, while retaining all spatial and property information.

The data can be seen to comprise primarily of vertically spread populations at fixed declination angles. Each column of data points in the plot in Fig. 4c relates to points with the same orientation, often referring to a singular grain but occasionally multiple grains with the same shared orientation. Within these grains, there is then a spread of hardness data, arising from other contributing factors to hardness, as well as measurement noise.

There are two primary contributions to the noise in this dataset: the misattribution of pixels between maps, and the physical influence of grain boundaries on nanoindentation hardness. The first is a result of the error in transforming the EBSD data and aligning it onto the hardness map, which will be discussed further in Discussion and Limitations. This error will occur in points lying close to grain boundaries: when overlaid, some pixels may contain the hardness data of one grain but the EBSD data of the adjacent grain due to misalignment. The second is due to the real effect that indents close to grain boundaries respond differently to indents performed in the centre of grains. Plastic zones that impinge upon grain boundaries can cause dislocation pile-up and slip transmission, or the grain boundary might act as a dislocation source/sink itself, strongly affecting measured hardness [50–56]. In order to avoid the influence of grain boundary-associated variation, and capitalising on the wealth of data available, points can be isolated based on spatial location relative to the microstructure. The EBSD data contain information on grain boundary location, and this can be used to calculate the distance of every indent to its nearest grain boundary, shown in Fig. 5.

The above scatter relationship can then be plotted excluding all points that lie near grain boundaries—this ensures that points are only plotted if they can confidently be assigned their orientation, and are unlikely to be impacted by the nearby grain boundary.

Figure 5d shows the scatter plot excluding all points within 7 μm of a grain boundary, with Fig. 5b showing the remaining points on the original nanoindentation map. These figures

contain 6246 data points, representing still a significant dataset, and the trend in Fig. 5d is significantly clearer than in Fig. 5c.

A simple, arbitrary functional form that fits the boundary conditions of the data has been selected and used to fit the data in Fig. 5d and is found to give a reasonable representation of the trend. It can be reasonably said that the remaining scatter within the data is largely a consequence of measurement noise in nanoindentation data at about 10%. This fitted relationship can be used to improve the spatial alignment of EBSD and nanoindentation datasets. The measured nanoindentation hardness values were used with the fitted relationship to produce a ‘simulated’ declination angle map. The simulated map does not contain all the crystallographic information within the EBSD data, but abrupt changes in the effective declination angle clearly demarc some of the grain boundaries in a similar way to that evident in the EBSD data. A Sobel edge detection filter [57] was applied to the EBSD, and hardness-derived simulated declination angle maps, to produce the maps shown in Fig. 13 (Supplementary Information).

These were used within an enhanced correlation coefficient (ECC) cross-correlative image alignment procedure [58, 59] to determine a homographic correction, allowing for two more degrees of freedom and capturing a greater range of distortions [60]. This further correction to the transformation from the spatial frames of the EBSD to nanoindentation data is now based on the extent of over-lapped fields, rather than a small number of discrete user-defined control points. The scatter plot and best fit relationship through the hardness and EBSD-measured declination angle shows only very minor changes for points remote from the grain boundaries after this correction to the spatial alignment. From this, the same structure–property scatter plot can be obtained with more confidence in the assigned orientation for each point.

Following this correction to the spatial alignment, the behaviour near grain boundaries can be explored with more confidence. The EBSD-measured declination angle at each pixel is used within the fitted relationship to determine the hardness expected for a grain in this orientation. The measured hardness map and the expected hardness calculated from crystal orientation are compared in Fig. 6a and b. This expected hardness is based on a fit to data obtained well away from grain boundaries, and benefits from lower noise due to the smoothing/averaging inherent in the data fitting process.

Variations in measured hardness across the microstructure can be made more apparent by subtracting the expected hardness from the measured hardness to give what will be referred to as the normalised hardness. This removes the quite marked (> 1 GPa) grain-to-grain hardness variation caused by orientation (Fig. 6a and b), leaving more subtle small variations visible in the normalised hardness map (Fig. 6c). In this case, we expect

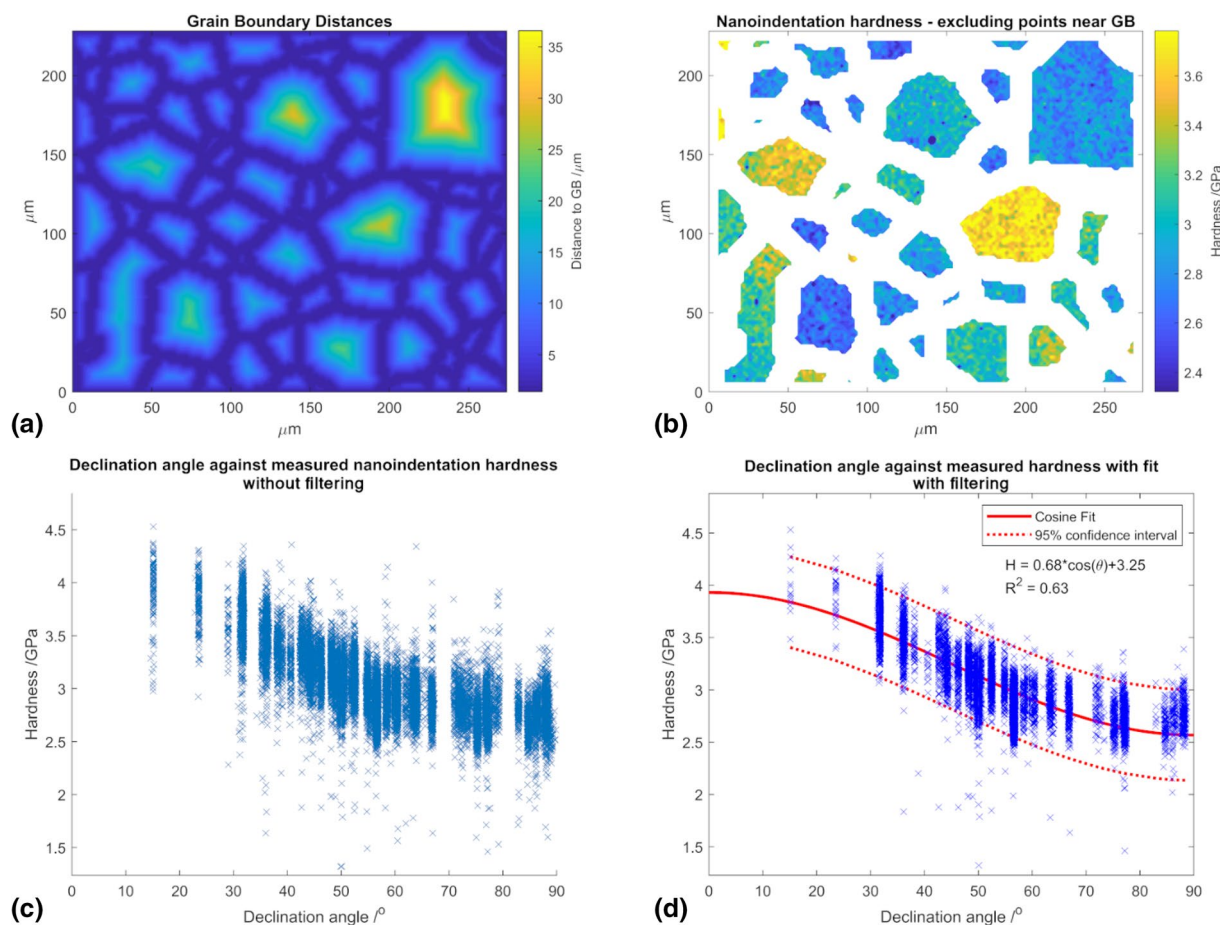


Figure 5: (a) Distances to grain boundaries obtained through the EBSD map, (b) the nanoindentation obtained hardness map excluding points in (a) with a value below 7 μm , (c) the scatter plot of declination angle, measured through EBSD, plotted against hardness measured through nanoindentation mapping as seen in Fig. 4, and (d) the scatter plot of (c), excluding all points that lie within 7 μm of a grain boundary as determined by EBSD with an arbitrary simple function fitted. 6246 data points are shown in (c). A 95% confidence interval is shown in the plot.

only secondary signals: noise, grain boundary effects, and possible chemical heterogeneities (though these have not been shown to be of concern in CP titanium).

Grain boundaries are clearly highlighted in the normalised hardness map (Fig. 6c). Some segments show higher measured nanoindentation hardness, while others show lower measured hardness. There are clear effects from noise, as well as from small deviations in nanoindentation positioning: horizontal stripes can be seen, resulting from overlapping indents and their resulting plastic zones due to stage misalignment. Some individual grains have a slightly higher mean normalised hardness, and others lower. Possible explanations for this variation include the approximate form of the assumed fitting function, as well as explanations with a physical basis, such as interactions with close sub-surface grain boundaries, or grains that may have high residual stresses due to cooling [28]. It is clear, however, that a primary source of variation in the normalised hardness is due to grain boundary effects. This can be visualised, as shown in Fig. 6d, as normalised hardness as a function of the distance to the grain

boundary, showing an increased divergence in normalised hardness in the vicinity of the grain boundary. The details of this, and further results, will be discussed in a further publication.

Dataset 2

To demonstrate further the capabilities of this method the second example also includes chemical information, and is a study of an oxygen diffusion layer generated on a CP titanium specimen that had been subjected to 230 h at 700 °C in air (Specimen 2). Figure 7 shows, from left to right, the EBSD obtained declination angle map, the EPMA obtained oxygen concentration map, and the nanoindentation hardness map. All maps have been registered using four user supplied control points to define two affine transformations mapping the EBSD and EPMA spatial data to that of the nanoindentation map.

The EBSD map shows that there is a strong texture element in this region of the specimen: there is a narrow distribution of grain declination angle. This keeps the specimen

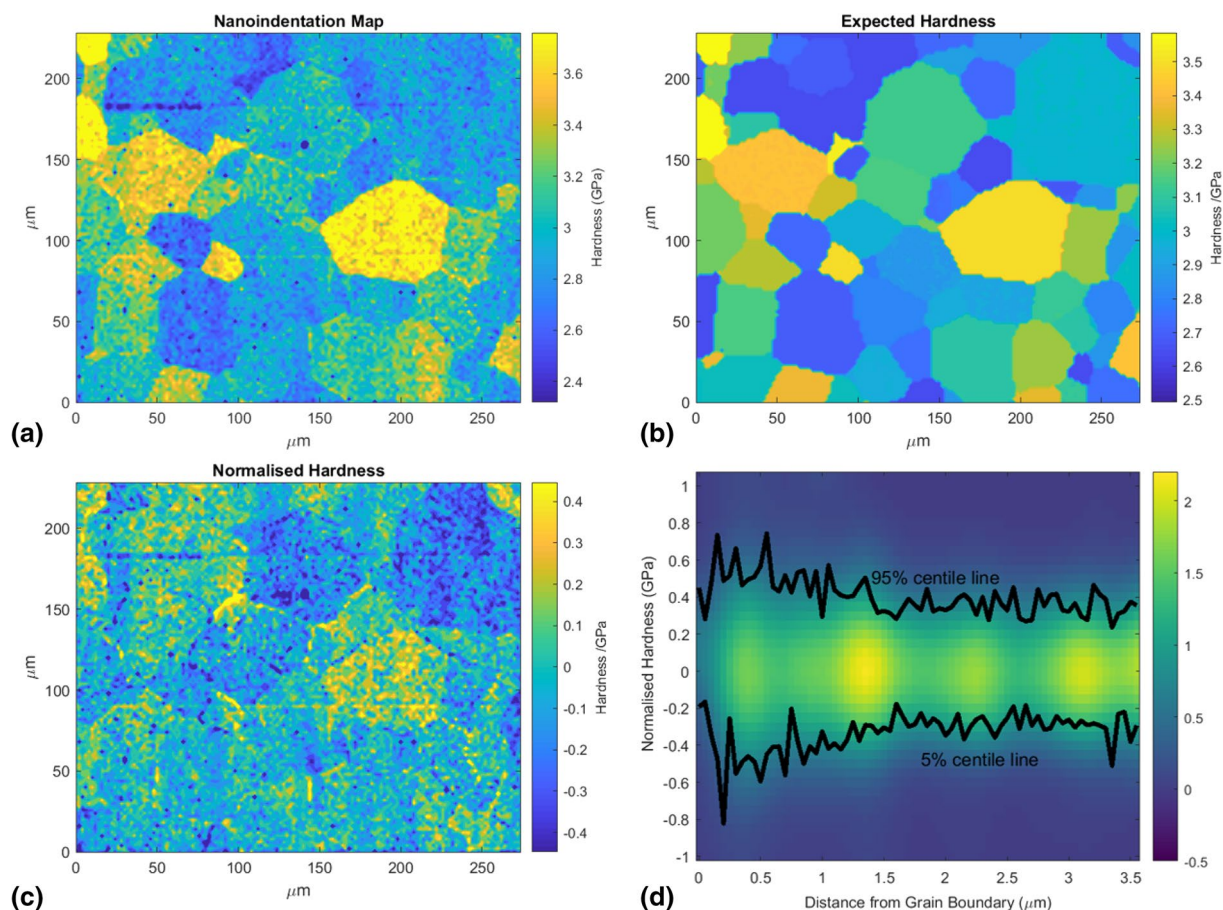


Figure 6: (a) Nanoindentation measured hardness, (b) expected hardness through the registered EBSD dataset and obtained relationship, (c) normalised hardness through subtraction of (a and b), (d) normalised hardness as a function of distance to the grain boundary. The colour scale in (d) indicates $\log(1 + N)$ where N is the number of indents at each combination of normalised hardness and distance from a grain boundary, while the lines show the 5th and 95th percentile values from normalised hardness distributions for indents at different distances from grain boundaries.

largely at the same orientation, allowing collection of a large dataset to study the relationship between hardness and oxygen content. Similarly to Specimen 1, it remains possible to observe the relationship between the nanoindentation hardness and the declination angle. Figure 14 (Supplementary Information) compares data found in this near surface layer to the trendlines established for Specimen 1.

These data show that a low number of orientations are probed within this region, and that there is a significant spread of hardness at a given orientation, with hardness reaching very high values of 20 GPa – four times the lower range of data points which are more in line with hardness levels measured in sample 1. The reason for this spread towards higher hardness values, clearly, is that this graph omits any information regarding oxygen content. The EPMA map in Fig. 7 shows that data points with high oxygen content can be excluded by considering points deeper than $\sim 120 \mu\text{m}$. For this subset, the average hardness is 3.0 GPa much more in line with the data

presented in Fig. 5d for the bulk Specimen 1, though with declination angles restricted to the range $60^\circ\text{--}90^\circ$.

Since both oxygen content and grain orientation vary, it is helpful to create a 3D plot of hardness versus oxygen content (from EPMA) and declinations angle (from EBSD) as is shown in Fig. 8.

It is clear from Fig. 8 that the spread in hardness in Fig. 14 is much more significantly correlated with the elevated and varying oxygen concentration, rather than crystal declination which is restricted to a relatively limited range, and is known from Fig. 5d to have a smaller effect on hardness. This graph shows that hardness increases as a function of oxygen concentration, as described in the literature [61], and can be fitted with a power-law function as done in Chen et al. [62]. A unique feature of this curve is the presence of a dip in hardness at approximately 13 units of oxygen measured. As we retain information on spatial information of each of these points, we can locate every point that lies below the 95% confidence interval, shown

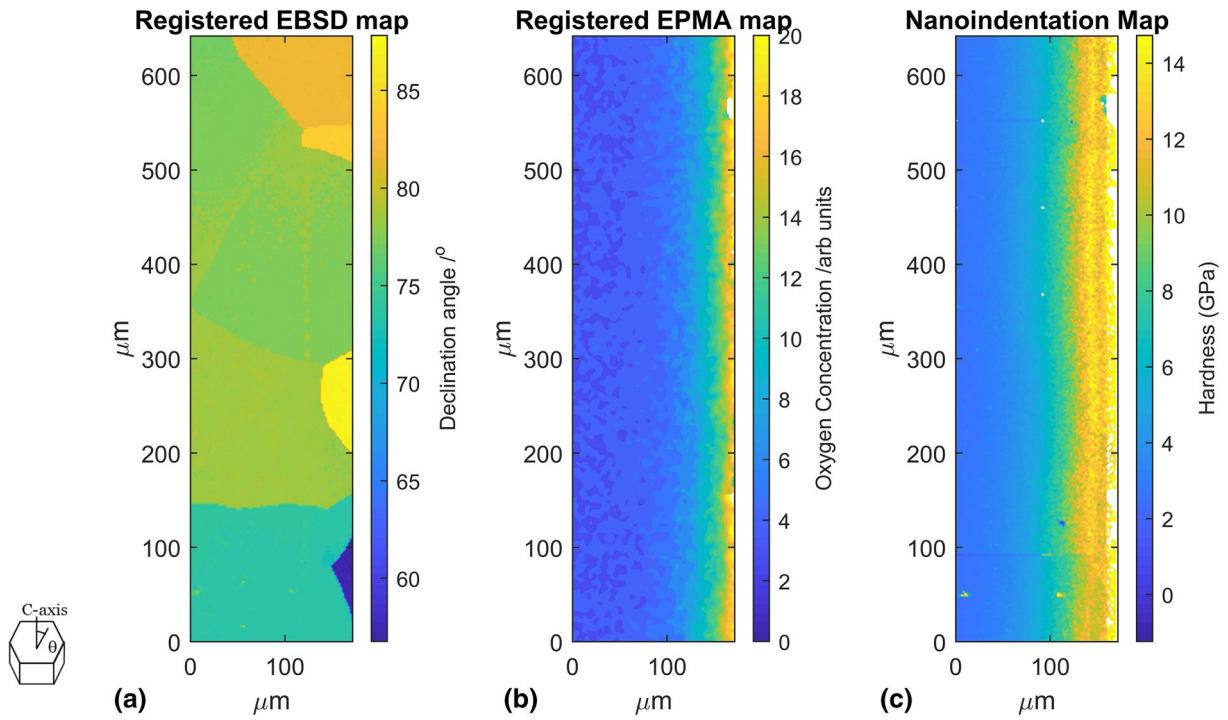


Figure 7: Dataset 2 represented as (a) EBSD map showing declination angle, (b) EPMA map showing oxygen concentration, and (c) nanoindentation map showing measured hardness.

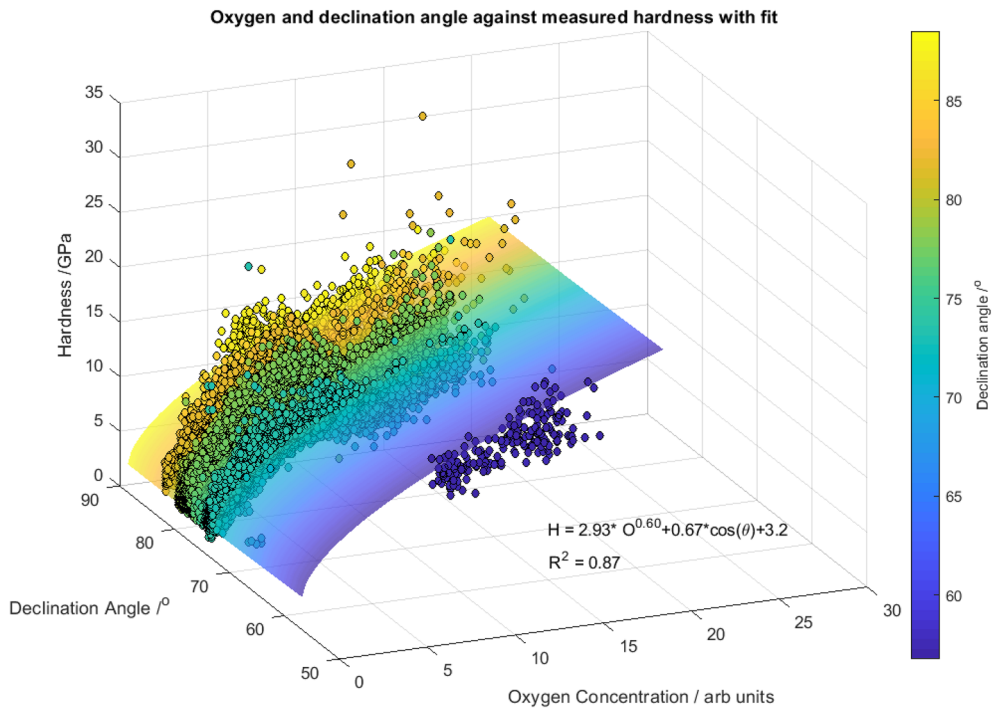


Figure 8: EBSD obtained declination angle against EPMA oxygen abundance against measured nanoindentation hardness. A total of 22,586 data points are shown. A fit with a combination of the orientation component obtained from Dataset 1, as well as a power exponent fitted via least-squares regression, is included. For ease of visualisation, points (and fitting surface) are coloured by the declination angle.

in Fig. 16 (Supplementary Information). These points all lie in a narrow band near the surface, where the oxygen concentration is highest. The reason for this dip in hardness is unclear, but it could be a surface effect or could be linked to the higher oxygen concentration in this region. The scatter plot of oxygen concentration against hardness is shown in Fig. 15 (Supplementary Information).

The ability to preserve, for every point, both spatial information and orientation information allows us to separate these source signals. In the case of grains, we can observe oxygen–hardness relationships for each set of orientations individually, shown as the different colourations in Fig. 8. We can also understand the clustering of data points in this plot as the inherent spatial positioning of the grains: notably the grain at 58° of declination angle does not extend beyond approximately 30 μm from the surface, leading to no points of that orientation having bulk levels of oxygen.

It can be seen that this technique rapidly provides us with orientation informed oxygen diffusion layer hardening information for this CP titanium system via the collection and alignment of three maps. Use of this technique can be extended to study more complex microstructural and chemical systems, enabling industrially motivated questions to be answered. For example, work by Gardner et al. [63] uses correlative hardness mapping, EPMA, EBSD, and atom probe tomography to quantify the effect of oxygen ingress on micromechanical properties of an in-service jet engine compressor disc.

Discussion and limitations

Reliability of input information

The rapid indent testing (3.5 s/indent) used for the nanoindentation mapping generates some limitations to the data generated. The most significant of these is the current limitation to analysis of hardness data. This decision was taken in part due to some further testing required to understand the details of the modulus calculations, as well as the lack of modulus contrast in a material that is known to produce these variations. Hardness data from nanoindentation mapping also contains a significant noise level with variations exceeding 10% of the average value obtained, likely due to the rapid nature in which it is collected.

The spatial alignment of nanoindentation mapping must also be considered. It can be seen from the resulting maps that rows of indents near the edge of a bundle occasionally overlap with neighbouring bundles, as a result of small stage misalignment. This is particularly noticeable in high spatial-resolution nanoindentation mapping, and can adversely affect data quality. Along these rows of indents, there can be significant changes in depth–spacing ratios, and in extreme cases include indents overlapping entirely, with an example shown in Fig. 17 (Supplementary Information). These effects are typically seen when

the indent spacing approaches the accuracy limit of the stepper motor used to drive the larger movements of the sample between bundles. Where the stepper motor makes slightly larger spacing between bundles, this does not influence the hardness values but will cause a slight dis-registry with spatial locations in the other maps.

A discussion of the details and limitations of the other input methods used in this paper can be found in previous publications related to those methods in particular [19, 64–68].

Reliability of analysis

The limitations of the analysis can also be split into two categories: alignment and interpolation. The first is an issue of error arising from the user input of reference points. A small change of a few pixels in one of the reference points can lead to significant changes to the affine transformation, particularly at the corners of the map and when maps have a high aspect ratio. This could lead to the misattribution of data points as being in the wrong grain. In an attempt to quantify the extent of such issues, the EBSD and nanoindentation maps of dataset 1 were registered multiple times using freshly input control points marked by the same observer. On average $4.3 \pm 1.0\%$ of pixels were assigned different grains when pairs of registered datasets were compared. When the additional full field ECC alignment was used, then $3.9 \pm 0.5\%$ of pixels were assigned to different grains.

The second is the question of interpolation. Datasets with discrete boundaries, such as in EBSD, must be interpolated with “nearest-neighbour” methods in order to avoid the fabrication of non-existent orientation data: grain boundaries are discrete, and a point interpolated as any average of points across the boundary is unphysical. However, this discrete nature of the grain assignment often causes stepped or serrated grain boundaries, and amplifies the errors in alignment discussed above.

Despite these limitations, the method presented provides a large quantity of data which can confidently be said to be well assigned, showing trends with high fidelity and data quantity.

Quantitative results

The structure–property relationships obtained show strong agreement with those collected and discussed in the literature before. Britton et al. [20] have reported the extent of anisotropic response of nanoindentation in CP titanium, with largely similar results in hardness data. However, as mentioned, the values of hardness and modulus collected via nanoindentation mapping have yet to be robustly compared to conventional CSM data, which may justify the relative difference in hardness values as well as our lack of modulus data.

The relationships obtained between nanoindentation hardness and oxygen, fitted with the same power-law function

as described in Zheng et al. [62], broadly agree with the literature [61, 69]. Without exact quantification of the oxygen signal, it is impossible to draw further conclusions from this, and further work aims to obtain reference points for these curves in order to quantify absolute measurement of oxygen weight percentages.

Finally, secondary effects such as grain boundary hardening can be seen, much in agreement with experiments in the literature showing variation in nanoindentation hardness in the vicinity of grain boundaries up to several microns in distance [52, 54], as well as the sensitivity of this variation to the crystal orientation of both grains [55, 56, 70, 71]. Results in the further analysis of these results to determine the underlying mechanism for this will be discussed in further publications.

Conclusion

Nanoindentation mapping has recently become an available tool for the collection of a large number of indents in a short time (e.g. dataset 1—15,870 points in 15 h). This has allowed for spatially resolved maps displaying mechanical properties, and providing datasets that are larger than have been previously obtainable.

Current literature showcases the utility of nanoindentation mapping through examples illustrating the ability to separate discrete phases and obtain statistically significant datasets of hardness and modulus for individual phases with large difference. This is work which otherwise would have required a targeted approach. However, until now there has been a challenge in determining results from continuous variables, such as crystallographic anisotropy, as it requires a separate source signal to be collected and properly registered.

This work demonstrates that when nanoindentation mapping is used in combination with other source signals, and correctly registered, rapid collection of structure property relationships with more subtle or continuous variables can be obtained.

Furthermore, we have shown that it is possible to deconvolve the effect of multiple varying structural properties on the mechanical response to nanoindentation, and clearly observe secondary effects such as grain boundary hardening. This paper presents the method for doing so, as well as highlighting the current limitations of nanoindentation mapping, the work required for registration of separate source signals, and the results obtainable with two standard use cases. Future work will endeavour to explore the more subtle variations observed, such as grain boundary hardening, as well as examine more complex use cases with strong industrial interest, such as oxygen diffusion in titanium alloys.

Methods

Sample preparation

Some preliminary measurements (dataset 0) were obtained from a fused silica sample, often used as a calibration material system for nanoindentation. The sample had been supplied by Goodfellow Ltd. and was used as polished.

Two specimens of grade 1 commercially pure titanium, supplied by Timet UK Ltd., were prepared for this experiment with an approximate size of $5 \times 5 \times 10$ mm. The chemical compositions of these, in weight percent, were 0.07 oxygen, 0.035 iron, 0.012 carbon, 0.0035 nitrogen, and the remainder titanium [72]. For Specimen 1, experiments were performed without further heat treatment to the material. For Specimen 2, one face was polished to 4000 grit with silicon carbide paper in order to create a uniform surface, and the specimen was subjected to 700 °C for 230 h in lab atmosphere to form an oxygen diffusion layer [62, 73]. Following this, Specimen 2 was cross-sectioned with a diamond saw blade in order to expose the oxygen diffusion profile.

Both specimens were mounted in Bakelite™, progressively ground to 4000 grit with silicon carbide paper, and finally polished with a colloidal silica suspension until clear grain contrast became visible under a polarised light microscope. In the case of Specimen 2, the edge which was to be examined was polished as the trailing edge, in order to ensure good edge retention.

In Specimen 1, a region of good quality polish towards the centre of the specimen was analysed, and in Specimen 2 the region analysed was selected at the surface such that it contained the full oxygen diffusion profile. Each region of interest was demarcated by nanoindents or otherwise recognisable features, and maps were taken of the same approximate region in the following order: an EPMA map, an EBSD map, and a nanoindentation map. This sequence was chosen to minimise the effect of one measurement method onto the other: nanoindentation mapping as the most surface-destructive was performed last, and EPMA which can be affected by the deposition of carbon contamination during EBSD was done first. The carbon contamination deposited via electron beam has been shown in preliminary experiments not to significantly affect nanoindentation readings performed at a depth of at least 100 nm.

EPMA mapping

EPMA maps for Specimen 2 were acquired on a CAMECA SX5-FE, located in the Oxford Dept. of Earth Sciences, equipped with five wavelength dispersive X-ray detectors. Conditions used were 10 keV accelerating potential, 15 nA beam current, 0.1 s dwell time per pixel, and 500 nm step size. Liquid nitrogen was used throughout the analysis to keep the levels of carbon contamination down. This was done not only to decrease the issues

with C contamination for the subsequent EBSD and nanoindent maps, but carbon build-up during long analyses has been shown to adversely affect the EPMA signal at the low accelerating potentials used here [65]. To further keep contamination level down while maximising the X-ray signal, maps were not acquired with a background pass. Background corrected test maps conducted on regions adjacent to the final maps showed no change in the background signal for any of the X-rays of interest.

X-ray signals collected were O-K α simultaneously collected on two WDS spectrometers using PC0 diffracting crystals, Ti K α simultaneously collected on two WDS spectrometers using LPET diffracting crystals, and N-K α collected using the PC2 diffracting crystal. O-K α and Ti-K α signals collected simultaneously were summed to increase the signal-to-noise. Note that we only report relative differences in composition due to the oxide surface layer present on the sample surface.

EBSD mapping

EBSD data were collected on a Zeiss Merlin FEG-SEM at a beam energy of 15 and 20 keV for Specimens 1 and 2, respectively, with a probe current of 10 nA. A Bruker e-Flash HR EBSD detector operated by Esprit 2.0 software was used acquire the EBSD maps with patterns collected and saved at a resolution of 150 \times 150 pixels. For Specimen 1, the mapped area was 460 μ m by 620 μ m at a step size of 0.8 μ m, while for Specimen 2 a 420 μ m by 1470 μ m region was mapped at 1 μ m spacing. The resolution and sampling density of both EPMA and EBSD is sufficiently high to identify relevant features such as grain morphology and oxygen profiles, and these are collected such that they are higher resolution than the nanoindentation maps. A discussion of this will follow in the analysis section.

Nanoindentation mapping

An Agilent Technologies (now KLA Tencor) G200 nanoindenter system was used to collect nanoindentation maps using the Express Test option. This instrument can perform 1 indent approximately every 3.5 s allowing for the collection of thousands of indents overnight. These indents are performed in a regular array, creating a map where every pixel corresponds to one indent. The collection strategy combines a piezo stage for high-resolution spatial accuracy across small areas and a stepper motor geared stage to allow for large collection areas, albeit with relatively lower positional accuracy. As such, the overall array is formed of a collection of sub-arrays, herein named “bundles”, within which the piezo stage controls position. The stepper motor movements are used to locate the centre of each bundle, allowing them to be stitched together. A graphical representation of this map-population strategy is shown in Fig. 9.

For each indent, the output data are values for maximum depth, load, modulus, hardness, and contact stiffness, instead of the conventional load–displacement curves collected in continuous stiffness measurements (CSM) [74, 75]. Though the load–displacement curve is not saved by the software in order to reduce file size, the modulus is calculated “on-the-fly” through the Oliver and Pharr method using a power-law fit on the unloading portion of the load–displacement curve [1]. The hardness is calculated through this stiffness-corrected contact depth using the same method [1]. This is in contrast to the more conventional CSM method used to validate measurements, possibly leading to the variations seen in these results.

Prior to discussions of analysis, the effect of thousands of indents on tip wear and calibration was considered. It is advisable for tip area functions to be re-calibrated regularly, either through direct means via AFM measurement or indirect means via indentation in reference material [76]. In common practice, this would often occur after several hundred indents had been performed at most, a time-scale which could span several months. However, nanoindentation maps can often contain orders of magnitude larger number of indents, with no opportunity to calibrate during data collection. We experimentally verify if tip area functions obtained through calibration on reference materials persist throughout several tens of thousands of indents. To illustrate this, an indentation map of over 33,000 indents was performed on fused silica with a maximum load of 3 mN, spaced 1.5 μ m apart. This corresponds to a depth/spacing ratio of \sim 1:10, with indents approximately \sim 150 nm deep. This was preceded and followed by two sets of nine CSM nanoindents to a target depth of 2000 nm. These were performed with an indentation strain rate of 0.05 s $^{-1}$, with a harmonic oscillation of 2 nm at 45 Hz, parameters used for all other CSM tests in this study. The first of these sets was used for tip area function calibration, using the software’s default analytical method with parameters as set out in Table 1.

Further to the tip calibration persistence test described above, a series of nanoindentation mapping tests were performed at depths of 100, 200, and 500 nm and compared to slower, conventional CSM tests at equivalent depths. The

TABLE 1: Parameters used during software calibration of tip area function through CSM indents on fused silica.

Parameter	Value/range
Range of depth for area calculation	50–2000 nm
Nominal modulus of tested material	Fixed at 72 GPa
Range of depth for load frame stiffness calculation	1500–2000 nm
Coefficient count	9, allowing negative
Lead term for area function	Unfixed
Analytical model: beta and epsilon	1.00, 0.75 (default) [80]

nanoindentation maps in these tests were conducted at a depth-to-spacing ratio of 1:10 (a discussion of this choice is given in “Results” section). In Specimen 1, the nanoindentation map was performed at a fixed load of 3 mN, corresponding to an approximate depth of 200 nm, with an indent spacing of 2 μm . In Specimen 2, the nanoindentation map was performed at a fixed load of 2.5 mN, corresponding to an approximate depth of 150 nm, with an indent spacing of 2 μm .

Analysis methodology

The analysis method presented correlates spatially resolved property maps on a pixel-by-pixel basis. An experimental and analytical challenge lies in the correct registration of property maps obtained across a wide variety of means. In particular, aligning EBSD signal maps onto nanoindentation maps presents a challenge due to the marked difference in the method of signal collection. Though tilt correction is applied, EBSD collection is performed with electron beam incidence angle of 70 degrees, and a small angular deviation between the two reference frames on the specimen can lead to significant misalignment across maps [77]. In order to resolve this, geometrical transformations and interpolation are used to map all datasets onto the same grid of coordinates. The method presented takes the X and Y coordinates of the nanoindentation maps to be the most accurate coordinate frame.

The transformations are carried out individually, relating all other property maps to the nanoindentation map. Fiducial markers or easily identifiable features act as reference markers across the maps, and an affine transformation is performed on the property map to be registered. The use of the affine transformation assumes the presence of solely linear distortions in all other property maps, i.e. that all distortions are as a result of geometrical projections from collection angles. This implies that the distortion can be described as the sum of x and y translation, scaling, rotation, and shear alone. It is recognised that other non-linear sources of distortion may be present. For example, mechanical drift during EBSD mapping could be non-linear. However, we observe that affine transformation accounts for the majority of discrepancy between mapping modalities used here at their current resolutions and collection timings. The best fit affine transformations required to map the positional EBSD and EPMA data onto the nanoindent reference axes were established by user identification of multiple corresponding points (at least four) within each dataset.

Following this, all property maps were interpolated in order to be scaled into an array the same size as the nanoindentation map. This often reduces the size of the dataset as nanoindentation mapping is not as high resolution as EBSD or EPMA, but retains the confidence that information obtained from correlations arises from real indents performed on the

local material at that point. A “nearest-neighbour” interpolation was used for EBSD datasets to avoid interpolating grain boundaries as smooth transitions, while a “linear” interpolation was used for EPMA maps as we expect smooth diffusion gradients.

The same process can be applied to any further property map taken: the position information is transformed, and the property data interpolated appropriately such that a stack of maps is produced, each pixel containing a vector of property information for a given location. It is then possible to correlate individual property pairs by threading through the stack of maps.

Acknowledgments

CMM would like to acknowledge financial support from the EPSRC, Rolls-Royce plc, and the Royal Commission for the Exhibition of 1851. CMM would also like to extend gratitude to advisors at Rolls-Royce plc including Prof D. Rugg, and Dr A. Radecka, as well as the advice and services offered at the David Cockayne Centre for Electron Microscopy in the University of Oxford.

Author contributions

CMM: Conceptualisation, Methodology, Software, Validation, Formal Analysis, Investigation, Data Curation, Writing, Visualisation. HMG: Methodology, Investigation, Validation. IH: Conceptualisation, Software. PG: Methodology, Investigation, Validation, Writing. JCW: Methodology, Validation. DR: Supervision, Project Administration, Funding Acquisition. DEJA: Conceptualisation, Project Administration, Funding Acquisition. AJW: Supervision, Conceptualisation, Formal Analysis, Writing, Project Administration, Funding Acquisition.

Data availability

A step-by-step guide is shown in the results of the first dataset. The code used for this analysis was written in MATLAB[®] [78], using the MTEX toolbox for EBSD importation [79]. The code necessary to reproduce these results uploaded to a GitHub Repository named “XPCorrelate” under an MIT License: <https://github.com/cmmagazz/XPCorrelate>.

Supplementary information

The online version contains supplementary material available at <https://doi.org/10.1557/s43578-020-00035-y>.

Open access

This article is licensed under a Creative Commons Attribution 4.0 International License, which permits use, sharing, adaptation, distribution and reproduction in any medium or format,

as long as you give appropriate credit to the original author(s) and the source, provide a link to the Creative Commons licence, and indicate if changes were made. The images or other third party material in this article are included in the article's Creative Commons licence, unless indicated otherwise in a credit line to the material. If material is not included in the article's Creative Commons licence and your intended use is not permitted by statutory regulation or exceeds the permitted use, you will need to obtain permission directly from the copyright holder. To view a copy of this licence, visit <http://creativecommons.org/licenses/by/4.0/>.

References

1. W.C. Oliver, G.M. Pharr, An improved technique for determining hardness and elastic modulus using load and displacement sensing indentation experiments. *J. Mater. Res.* **7**(6), 1564–1583 (1992)
2. J. Gong, A.J. Wilkinson, Micro-cantilever testing of a prismatic slip in commercially pure Ti. *Philos. Mag.* **91**(7–9), 1137–1149 (2011)
3. J. Gong, A.J. Wilkinson, A microcantilever investigation of size effect, solid-solution strengthening and second-phase strengthening for $\langle a \rangle$ prism slip in alpha-Ti. *Acta Mater.* **59**(15), 5970–5981 (2011)
4. M. Quaresimin, Modelling the fatigue behaviour of bonded joints in composite materials, in *Multi-scale Modelling of Composite Material Systems*. ed. by C. Soutis, P.W.R. Beaumont (Woodhead, Cambridge, 2005), pp. 469–494
5. E. Le Pen, D. Baptiste, G. Hug, Multi-scale fatigue behaviour modelling of Al-Al₂O₃ short fibre composites. *Int. J. Fatigue* **24**, 205–214 (2002)
6. K. Sai, G. Cailletaud, Multi-mechanism models for the description of ratchetting: Effect of the scale transition rule and of the coupling between hardening variables. *Int. J. Plasticity* **23**, 1589–1617 (2007)
7. Y. Xiong et al., Cold creep of titanium: analysis of stress relaxation using synchrotron diffraction and crystal plasticity simulations. *Acta Mater.* **15**, 561–577 (2020)
8. Y. Guo, D.M. Collins, E. Tarleton, F. Hofmann, A.J. Wilkinson, T. Ben Britton, Dislocation density distribution at slip band-grain boundary intersections. *Acta Mater.* **182**, 172–183 (2020)
9. S. Das, F. Hofmann, E. Tarleton, Consistent determination of geometrically necessary dislocation density from simulations and experiments. *Int. J. Plasticity* **109**, 18–42 (2018)
10. E. Tarleton, S.G. Roberts, Dislocation dynamic modelling of the brittle-ductile transition in tungsten. *Philos. Mag.* **89**(31), 2759–2769 (2009)
11. A.L. Pilchak, The effect of friction stir processing on the microstructure, mechanical properties and fracture behavior of investment cast Ti-6Al-4V. PhD Thesis, The Ohio State University (2009)
12. A.L. Pilchak, J.C. Williams, The effect of friction stir processing on the mechanical properties of investment cast and hot isostatically pressed Ti-6Al-4V. *Metall. Mater. Trans. A* **42**(6), 1630–1645 (2011)
13. W.Y. Li et al., Microstructure characterization and mechanical properties of linear friction welded Ti-6Al-4V alloy. *Adv. Eng. Mater.* **10**(1–2), 89–92 (2008)
14. P. Frankel, M. Preuss, A. Steuwer, P.J. Withers, S. Bray, Comparison of residual stresses in Ti-6Al-4V and Ti-6Al-2Sn-4Zr-2Mo linear friction welds. *Mater. Sci. Technol.* **25**(5), 640–650 (2009)
15. C. Qiu et al., Influence of processing conditions on strut structure and compressive properties of cellular lattice structures fabricated by selective laser melting. *Mater. Sci. Eng. A* **628**, 188–197 (2015)
16. Y.M. Arisoy, L.E. Criales, T. Özel, B. Lane, S. Moylan, A. Donmez, Influence of scan strategy and process parameters on microstructure and its optimization in additively manufactured nickel alloy 625 via laser powder bed fusion. *Int. J. Adv. Manuf. Technol.* **90**(5–8), 1393–1417 (2017)
17. D.E.J. Armstrong, A.J. Wilkinson, S.G. Roberts, Measuring anisotropy in Young's modulus of copper using microcantilever testing. *J. Mater. Res.* **24**(11), 3268–3276 (2009)
18. F.J. Humphreys, Review Grain and subgrain characterisation by electron backscatter diffraction. *J. Mater. Sci.* **36**, 3833–3854 (2001)
19. T.B. Britton et al., Tutorial: crystal orientations and EBSD—or which way is up? *Mater. Charact.* **117**, 113–126 (2016)
20. T.B. Britton, H. Liang, F.P.E. Dunne, A.J. Wilkinson, The effect of crystal orientation on the indentation response of commercially pure titanium: Experiments and simulations. *Proc. R. Soc. A Math. Phys. Eng. Sci.* **466**(2115), 695–719 (2010)
21. D. Rugg, T.B. Britton, J. Gong, A.J. Wilkinson, P.A.J. Bagot, In-service materials support for safety critical applications—a case study of a high strength Ti-alloy using advanced experimental and modelling techniques. *Mater. Sci. Eng. A* **599**, 166–173 (2014)
22. F.F. Dear et al., Combined APT, TEM and SAXS characterisation of nanometre-scale precipitates in titanium alloys. *Microsc. Microanal.* **25**(S2), 2516–2517 (2019)
23. Y. Chang et al., Characterizing solute hydrogen and hydrides in pure and alloyed titanium at the atomic scale. *Acta Mater.* **150**, 273–280 (2018)
24. H.N. Southworth, Scanning electron microscopy and microanalysis, in *Physicochemical Methods of Mineral Analysis*. ed. by A.W. Nicol (Springer, Boston, MA, 1975), pp. 421–450
25. X. Llovet, A. Moy, P.T. Pinard, J.H. Fournelle, Electron probe microanalysis: a review of recent developments and applications

- in materials science and engineering. *Prog. Mater. Sci.* **116**, 100673 (2020)
26. A.J. Wilkinson, E.E. Clarke, T.B. Britton, P. Littlewood, P.S. Karamched, High-resolution electron backscatter diffraction: an emerging tool for studying local deformation. *J. Strain Anal. Eng. Des.* **45**(5), 365–376 (2010)
 27. T.B. Britton, D. Randman, A.J. Wilkinson, Nanoindentation study of slip transfer phenomenon at grain boundaries. *J. Mater. Res.* **24**, 607–615 (2017)
 28. D. Rugg, M. Dixon, F.P.E. Dunne, Effective structural unit size in titanium alloys. *J. Strain Anal. Eng. Des.* **42**, 269 (2007)
 29. T.S. Jun, D.E.J. Armstrong, T.B. Britton, A nanoindentation investigation of local strain rate sensitivity in dual-phase Ti alloys. *J. Alloys Compd.* **672**, 282–291 (2016)
 30. M. Mayo, R. Siegel, Y. Liao, W. Nix, Nanoindentation of nanocrystalline ZnO. *J. Mater. Res.* **7**(4), 973–979 (1992)
 31. H. Somekawa, C.A. Schuh, High-strain-rate nanoindentation behavior of fine-grained magnesium alloys. *J. Mater. Res.* **27**(9), 1295–1302 (2012)
 32. S. Shim, H. Bei, M.K. Miller, G.M. Pharr, E.P. George, Effects of focused ion beam milling on the compressive behavior of directionally solidified micropillars and the nanoindentation response of an electropolished surface. *Acta Mater.* **57**(2), 503–510 (2009)
 33. D.R.P. Singh, N. Chawla, G. Tang, Y.L. Shen, Micropillar compression of Al/SiC nanolaminates. *Acta Mater.* **58**(20), 6628–6636 (2010)
 34. S. Korte, R.J. Stearn, J.M. Wheeler, W.J. Clegg, High temperature microcompression and nanoindentation in vacuum. *J. Mater. Res.* **27**(1), 167–176 (2012)
 35. S. Korte, W.J. Clegg, Micropillar compression of ceramics at elevated temperatures. *Scr. Mater.* **60**(9), 807–810 (2009)
 36. E.M. Grieveson, D.E.J. Armstrong, S. Xu, S.G. Roberts, Compression of self-ion implanted iron micropillars. *J. Nucl. Mater.* **430**(1–3), 119–124 (2012)
 37. P. Sudharshan Phani, W.C. Oliver, A critical assessment of the effect of indentation spacing on the measurement of hardness and modulus using instrumented indentation testing. *Mater. Des.* **164**, 107563 (2019)
 38. B. Vignesh, W.C. Oliver, G.S. Kumar, P.S. Phani, Critical assessment of high speed nanoindentation mapping technique and data deconvolution on thermal barrier coatings. *Mater. Des.* **181**, 108084 (2019)
 39. E.D. Hintsala, U. Hangen, D.D. Stauffer, High-throughput nanoindentation for statistical and spatial property determination. *JOM* **70**(4), 494–503 (2018)
 40. M. Sebastiani, R. Moscatelli, F. Ridi, P. Baglioni, F. Carassiti, High-resolution high-speed nanoindentation mapping of cement pastes: Unravelling the effect of microstructure on the mechanical properties of hydrated phases. *Mater. Des.* **97**, 372–380 (2016)
 41. N.X. Randall, M. Vandamme, F.J. Ulm, Nanoindentation analysis as a two-dimensional tool for mapping the mechanical properties of complex surfaces. *J. Mater. Res.* **24**(3), 679–690 (2009)
 42. E.P. Koumoulos, K. Paraskevoudis, C.A. Charitidis, Constituents phase reconstruction through applied machine learning in nanoindentation mapping data of mortar surface. *J. Compos. Sci.* **3**(3), 63 (2019)
 43. C. Tromas, J.C. Stinville, C. Templier, P. Villechaise, Hardness and elastic modulus gradients in plasma-nitrided 316L polycrystalline stainless steel investigated by nanoindentation tomography. *Acta Mater.* **60**(5), 1965–1973 (2012)
 44. C. Tromas, M. Arnoux, X. Milhet, Hardness cartography to increase the nanoindentation resolution in heterogeneous materials: application to a Ni-based single-crystal superalloy. *Scr. Mater.* **66**(2), 77–80 (2012)
 45. D. Goldbaum, R.R. Chromik, N. Brodusch, R. Gauvin, Microstructure and mechanical properties of Ti cold-spray splats determined by electron channeling contrast imaging and nanoindentation mapping. *Microsc. Microanal.* **21**(3), 570–581 (2015)
 46. J.M. Wheeler, Mechanical phase mapping of the Taza meteorite using correlated high-speed nanoindentation and EDX. *J. Mater. Res.* (2020). <https://doi.org/10.1557/jmr.2020.207>
 47. K. Herrmann, N.M. Jennett, W. Wegener, J. Meneve, K. Hasche, R. Seemann, Progress in determination of the area function of indenters used for nanoindentation. *Thin Solid Films* **377–378**, 394–400 (2000)
 48. M.R. Bache, W.J. Evans, V. Randle, R.J. Wilson, Characterization of mechanical anisotropy in titanium alloys. *Mater. Sci. Eng. A* **257**(1), 139–144 (1998)
 49. T.B. Britton, F.P.E. Dunne, A.J. Wilkinson, On the mechanistic basis of deformation at the microscale in hexagonal close-packed metals. *Proc. R. Soc. A Math. Phys. Eng. Sci.* **471**(2178), 20140881 (2015)
 50. W.A. Soer, J.T.M. De Hosson, Detection of grain-boundary resistance to slip transfer using nanoindentation. *Mater. Lett.* **59**(24–25), 3192–3195 (2005)
 51. T.B. Britton, D. Randman, A.J. Wilkinson, Nanoindentation study of slip transfer phenomenon at grain boundaries. *J. Mater. Res.* **24**(3), 607–615 (2009)
 52. Y. Su, C. Zambaldi, D. Mercier, P. Eisenlohr, T.R. Bieler, M.A. Crimp, Quantifying deformation processes near grain boundaries in a titanium using nanoindentation and crystal plasticity modeling. *Int. J. Plasticity* **86**, 170–186 (2016)
 53. E. Bayerschen, A.T. McBride, B.D. Reddy, T. Böhlke, Review on slip transmission criteria in experiments and crystal plasticity models. *J. Mater. Sci.* **51**, 2243–2258 (2016)
 54. Y. Guo, T.B. Britton, A.J. Wilkinson, Slip band-grain boundary interactions in commercial-purity titanium. *Acta Mater.* **76**, 1–12 (2014)

55. S. Miura, Y. Saeki, Plastic deformation of aluminum bicrystals $\langle 100 \rangle$ oriented. *Acta Metall.* **26**(1), 93–101 (1978)
56. J. Kacher, I.M. Robertson, In situ and tomographic analysis of dislocation/grain boundary interactions in α -titanium. *Philos. Mag.* **94**(8), 814–829 (2014)
57. S. Sodha, An implementation of sobel edge detection. Project Rhea. https://www.projectrhea.org/rhea/index.php/An_Implementation_of_Sobel_Edge_Detection. Accessed 23 Jul 2020
58. G. Evangelidis, ECC image alignment algorithm (image registration). MATLAB Central File Exchange. <https://uk.mathworks.com/matlabcentral/fileexchange/27253-ecc-image-alignment-algorithm-image-registration>. Accessed 06 Apr 2020
59. G.D. Evangelidis, E.Z. Psarakis, Parametric image alignment using enhanced correlation coefficient maximization. *IEEE Trans. Pattern Anal. Mach. Intell.* **30**(10), 1858–1865 (2008)
60. S. Seitz et al., Homography, transforms, mosaics. New York.
61. H. Conrad, Effect of interstitial solutes on the strength and ductility of titanium. *Prog. Mater. Sci.* **26**(2–4), 123–403 (1981)
62. G.Z. Chen, D.J. Fray, T.W. Farthing, Cathodic deoxygenation of the alpha case on titanium and alloys in molten calcium chloride. *Metall. Mater. Trans. B Process Metall. Mater. Process. Sci.* **32**(6), 1041–1052 (2001)
63. H.M. Gardner et al., Quantifying the effect of oxygen on micro-mechanical properties of a near-alpha titanium alloy (2020)
64. D. Drouin, A.R. Couture, D. Joly, X. Tastet, V. Aimez, R. Gauvin, CASINO V2.42—a fast and easy-to-use modeling tool for scanning electron microscopy and microanalysis users. *Scanning* **29**(3), 92–101 (2007)
65. P. Gopon, J. Fournelle, P.E. Sobol, X. Llovet, Low-Voltage electron-probe microanalysis of Fe-Si compounds using soft X-rays. *Microsc. Microanal.* **19**(6), 1698–1708 (2013)
66. J.R. Goldstein, J. Newbury, D.E. Joy, D.C. Lyman, C.E. Echlin, P. Lifshin, E. Sawyer, L. Michael, *Scanning Electron Microscopy and X-Ray Microanalysis* (Springer, New York, 2003).
67. A.J. Wilkinson, T. Ben Britton, Strains, planes, and EBSD in materials science. *Mater. Today* **15**(9), 366–376 (2012)
68. S.J.B. Reed, *Electron Microprobe Analysis and Scanning Electron Microscopy in Geology* (Cambridge University Press, Cambridge, 2005).
69. H.M. Gardner, A. Radecka, D. Rugg, D.E.J. Armstrong, M.P. Moody, P.A.J. Bagot, A study of the interaction of oxygen with the $\alpha 2$ phase in the model alloy Ti–7wt%Al. *Scr. Mater.* **185**, 111–116 (2020)
70. J.D. Livingston, B. Chalmers, Multiple slip in bicrystal deformation. *Acta Metall.* **5**(6), 322–327 (1957)
71. J. Kacher, B.P. Eftink, B. Cui, I.M. Robertson, Dislocation interactions with grain boundaries. *Curr. Opin. Solid State Mater. Sci.* **18**(4), 227–243 (2014)
72. J. Gong, A.J. Wilkinson, Anisotropy in the plastic flow properties of single-crystal α titanium determined from micro-cantilever beams. *Acta Mater.* **57**(19), 5693–5705 (2009)
73. R. Gaddam, B. Sefer, R. Pederson, M.L. Antti, Study of alpha-case depth in Ti–6Al–2Sn–4Zr–2Mo and Ti–6Al–4V. *IOP Conf. Ser. Mater. Sci. Eng.* **48**(1), 012002 (2013)
74. J.B. Pethica, W.C. Oliver, Mechanical properties of nanometre volumes of material: use of the elastic response of small area indentations. *MRS Proc.* **130**, 13–23 (1988)
75. X. Li, B. Bhushan, A review of nanoindentation continuous stiffness measurement technique and its applications. *Mater. Charact.* **48**(1), 11–36 (2002)
76. M.A. Monclús, S. Lotfian, J.M. Molina-Aldareguía, Tip shape effect on hot nanoindentation hardness and modulus measurements. *Int. J. Precis. Eng. Manuf.* **15**(8), 1513–1519 (2014)
77. G. Nolze, Image distortions in SEM and their influences on EBSD measurements. *Ultramicroscopy* **107**(2–3), 172–183 (2007)
78. The MathWorks Inc., MATLAB version R2019a. The MathWorks Inc., Natick, MA (2019)
79. F. Bachmann, R. Hielscher, H. Schaeben, Texture analysis with MTEX- Free and open source software toolbox. *Solid State Phenom.* **160**, 63–68 (2010)
80. ISE/101/5, Metallic materials—instrumented indentation test for hardness and materials parameters—part 1: test method. *ISO* **3**(1), 27 (2002).